Orchestrating nonmuscle myosin II filament assembly at the onset of cytokinesis

Fereshteh R. Najafabadi[a,b,†], Mark Leaver[a,b,†], and Stephan W. Grill[a,b,c,*]
[a]Max Planck Institute of Molecular Cell Biology and Genetics, Pfotenhauerstrasse 108, Dresden 01307, Germany; [b]Biotechnology Centre, Technische Universität Dresden, Tatzberg 47/49, Dresden 01307; [c]Excellence Cluster Physics of Life, Technische Universität, Dresden 01307, Germany

ABSTRACT **Contractile forces in the actomyosin cortex are required for cellular morphogenesis. This includes the invagination of the cell membrane during division, where filaments of nonmuscle myosin II (NMII) are responsible for generating contractile forces in the cortex. However, how NMII heterohexamers form filaments in vivo is not well understood. To quantify NMII filament assembly dynamics, we imaged the cortex of *Caenorhabditis elegans* embryos at high spatial resolution around the time of the first division. We show that during the assembly of the cytokinetic ring, the number of NMII filaments in the cortex increases and more NMII motors are assembled into each filament. These dynamics are influenced by two proteins in the RhoA GTPase pathway, the RhoA-dependent kinase LET-502 and the myosin phosphatase MEL-11. We find that these two proteins differentially regulate NMII activity at the anterior and at the division site. We show that the coordinated action of these regulators generates a gradient of free NMII in the cytoplasm driving a net diffusive flux of NMII motors toward the cytokinetic ring. Our work highlights how NMII filament assembly and disassembly dynamics are orchestrated over space and time to facilitate the up-regulation of cortical contractility during cytokinesis.**

Monitoring Editor
Karen Oegema
University of California, San Diego

Received: Dec 3, 2021
Revised: Apr 14, 2022
Accepted: May 5, 2022

INTRODUCTION

A dynamic cytoskeleton can change a cell's shape including constricting the membrane during division—a process essential for life. Actomyosin is the cytoskeletal component involved in cell division in animal cells and is found in a thin layer called the cortex that underlies the cell membrane (Salbreux *et al.*, 2012; Blanchoin *et al.*, 2014). It consists of actin filaments cross-linked by the molecular motor nonmuscle myosin II (Pollard, 2016), hereafter referred to as NMII. NMII is a member of the myosin superfamily of motor proteins and functions by pulling on actin filaments to generate the force needed to deform the cortex during cell division (Sellers, 2000; Lecuit *et al.*, 2011). NMII is a heterohexamer consisting of two heavy chains, two essential light chains, and two regulatory light chains called the essential light chain and the regulatory light chain (ELC and RLC, respectively). The heavy chains hydrolyze ATP to cause a conformational change—called the power stroke—that pulls against actin. The two light chains regulate this activity (Sellers, 2000). Multiple NMII motor proteins assemble into bipolar filaments that can cross-link two actin filaments. The concerted action of NMII motors in such a filament generates force between two adjacent actin filaments (Levayer and Lecuit, 2012). Human NMII has been estimated to contain around 30 motors per filament (Niederman and Pollard, 1975; Billington *et al.*, 2013). However, the details of how the biochemistry of NMII results in the behaviors of the cortex at the cellular levels is not well understood.

Recent work, in our lab and others, considers the cortex as a thin-layer, active fluid and has applied hydrodynamic theory to describe

This article was published online ahead of print in MBoC in Press (http://www.molbiolcell.org/cgi/doi/10.1091/mbc.E21-12-0599) on May 11, 2022.
The authors declare no competing financial interests.
[†]These authors contributed equally to the work.
Data availability: Data and analysis routines will be made avaliable upon request.
Author contributions: F.R.N. performed all the experiments and data analysis for Figures 1–4 and Supplemental Figures S1 and S2 with help from S.W.G. and M.L.; M.L. performed data analysis for Figures 5–7 and Supplemental Figures 4–6; M.L. wrote the manuscript with help from F.R.N. and S.W.G.; F.R.N., M.L., and S.W.G. conceived the study.
*Address correspondence to: Stephan W. Grill (grill@mpi-cbg.de).
Abbreviations used: GFP, green fluorescent protein; MLC, myosin light chain; NA, numerical aperture; NMII, nonmuscle myosin II; PIV, particle image velocimetry; RLC, regulatory light chain; RNAi, RNA interference; ROI, region of interest; SGM, Shelton's growth media; SI TIRF, structured illumination total internal reflection fluorescence; v_x, cortical velocity along the AP axis.
© 2022 Najafabadi *et al.* This article is distributed by The American Society for Cell Biology under license from the author(s). Two months after publication it is available to the public under an Attribution–Noncommercial-Share Alike 4.0 International Creative Commons License (http://creativecommons.org/licenses/by-nc-sa/4.0).
"ASCB®," "The American Society for Cell Biology®," and "Molecular Biology of the Cell®" are registered trademarks of The American Society for Cell Biology.

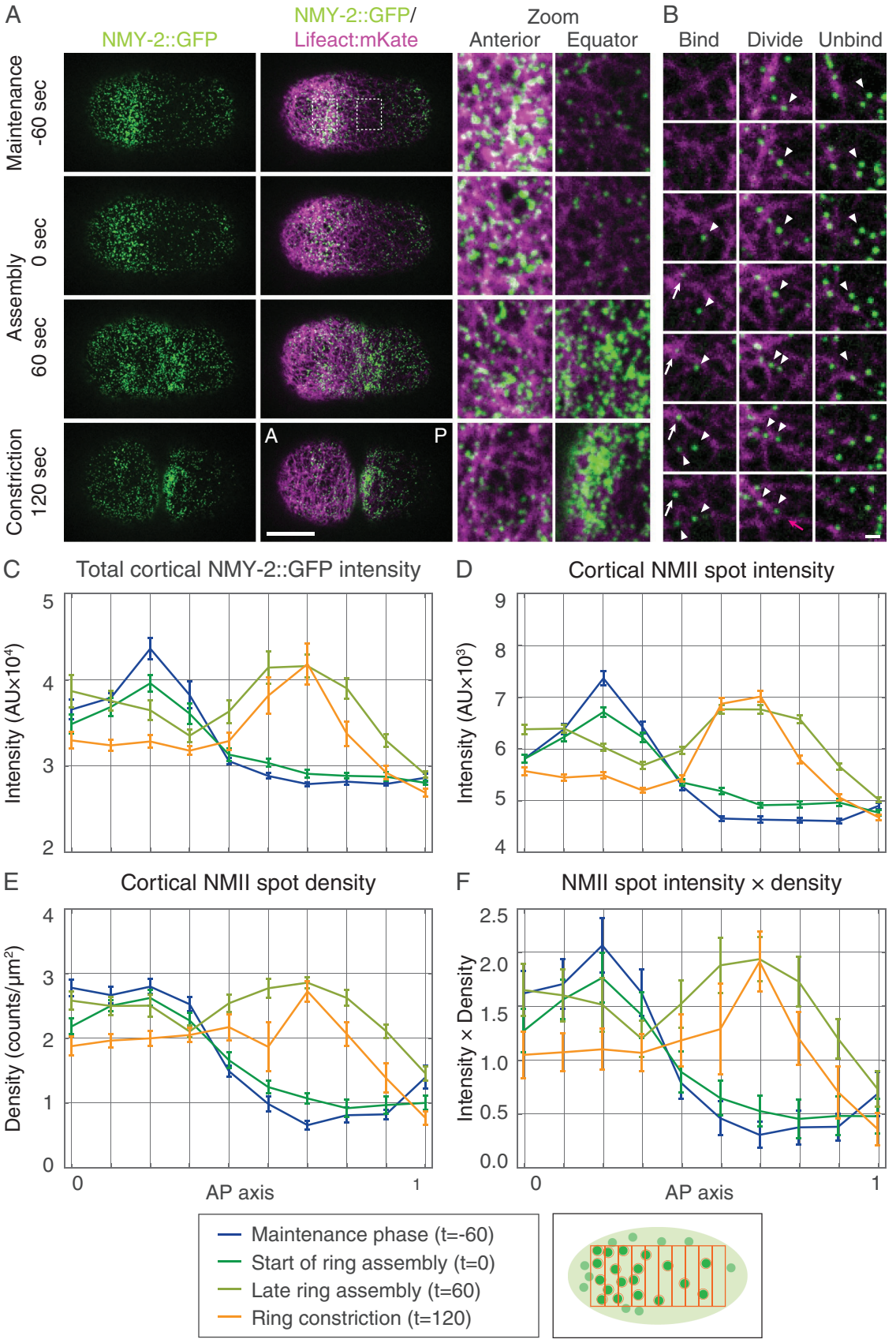

FIGURE 1: NMII spot dynamics at the cortex and changes in localization of NMY-2::GFP in the cell during the assembly of the ring. (A) Spinning-disk confocal microscopy images of *C. elegans* one-cell embryos labeled with NMY-2::GFP (green) and the marker for actin filaments, LifeAct::mKate (magenta). Representative images of cells during the maintenance phase ($t = -60$ s), assembly of the ring ($t = 0$–60 s), and cytokinesis are shown ($t = 120$ s). Two enlarged

its behavior (Salbreux *et al.*, 2009; Jülicher *et al.*, 2018). This approach has helped elucidate the role of NMII in the dynamic rearrangement of the cortex during early development, specifically in *Caenorhabditis elegans* (Mayer *et al.*, 2010; Naganathan *et al.*, 2014; Reymann *et al.*, 2016; Pimpale *et al.*, 2020). However, more detailed data, for example, on the assembly and disassembly dynamics of NMII filaments, are needed in order to arrive at more accurate theoretical descriptions of cortical dynamics.

In the one-cell *C. elegans* embryo, the cortex undergoes a series of rearrangements. At the end of the S-phase of first mitotic division (Begasse and Hyman 2011), the sperm enters at the posterior of the oocyte and inhibits myosin locally (Goldstein and Hird, 1996). This change in myosin concentration establishes a gradient of contractility in the cortex that induces it to flow from posterior to anterior (Motegi and Sugimoto, 2006; Gubieda *et al.*, 2020). Thus the uniformly distributed cortex is rearranged to form an accumulation of actomyosin at the anterior pole of the cell called the anterior cap (Schonegg and Hyman, 2006, Pacquelet, 2017). This change in the myosin distribution breaks the symmetry of the cell and sets the anterior-posterior axis. During the maintenance phase, the levels of actomyosin in the cortex are kept high in the anterior and low in the posterior (Rose and Gönczy, 2014; Kumfer *et al.*, 2010; Pacquelet, 2017). This phase corresponds to the prometaphase of the first cell division (Begasse and Hyman, 2011). The maintenance phase ends when the anterior cap disassembles and a contractile ring forms at the future position of the cytokinetic furrow (Tse *et al.*, 2011, 2012; Reymann *et al.*, 2016; Pacquelet, 2017). At this time, the neighboring cortex flows into the ring, which gives rise to shear flows and the ordering of actin filaments into parallel bundles. Force generation in the ring then pulls the membrane inward to divide the cell (Reymann *et al.*, 2016; Khaliullin *et al.*, 2018).

Different regulators of NMII activity control the various rearrangements of the cortex, including RHO-1 and the PAR polarity proteins. RHO-1 is the *C. elegans* ortholog of the RhoA GTPase—a molecular switch that regulates myosin contractility via phosphorylation of the myosin light chain called MLC-4 in *C. elegans* (Etienne-Manneville and Hall, 2002; Piekny and Mains, 2002). The PAR proteins form mutually antagonistic membrane domains that define the anterior and posterior sides of the cell (Hoege and Hyman, 2013). During flow phase, PAR polarity proteins and RHO-1 activate NMII (Jenkins *et al.*, 2006; Begasse and Hyman, 2011; Pacquelet, 2017) via the kinase LET-502, a member of the ROCK family of Rho-dependent kinases (Wissmann *et al.*, 1997; Piekny and Mains, 2002). During the maintenance phase, NMII levels are controlled by the PAR polarity proteins and CDC-42—another member of the Rho GTPase family (Motegi and Sugimoto, 2006; Schonegg and Hyman, 2006)—perhaps via its effector MRCK-1 (Beatty *et al.*, 2013; Marston *et al.*, 2016). During cytokinesis, signals from the spindle mid-zone and astral microtubules activate RHO-1 at the cortex to initiate the assembly of the cytokinetic ring (Dechant and Glotzer, 2003; Bringmann and Hyman, 2005; Wolfe *et al.*, 2009; Green *et al.*, 2012).

These regulated rearrangements of the cortex represent switches between periods of stability and dynamic change (Begasse and Hyman, 2011; Pacquelet, 2017). However, it is currently unclear if and how the dynamics of NMII motors induce these switches. Specifically, it remains elusive how NMII regulation is orchestrated in time and space. Specifically, we are interested in the dynamics of how NMII assembles into filaments and subsequently disassembles into free motors. The assembly of the ring therefore offers a good opportunity to investigate these dynamics: occurring after a period of stability—the maintenance phase—and before the onset of the cortical flows that transport cortical matter toward the equators (Maddox *et al.*, 2007; Reymann *et al.*, 2016; Khaliullin *et al.*, 2018). To investigate this, we looked at the dynamics of NMII motors in filaments in the cortex at high temporal and spatial resolution.

RESULTS

The dynamic rearrangement of the cortex at the cellular scale involves binding and unbinding of NMII

To investigate the dynamics of NMII during the assembly of the ring, we analyzed the localization of NMY-2 over space and time. To do this, we performed time-lapse imaging using spinning-disk microscopy. A strain expressing NMY-2 fused to green fluorescent protein (GFP; NMY-2::GFP) and the actin binding protein Lifeact fused to mKate2 (Lifeact::mKate, methods) was used to label actomyosin. We first considered the distribution of NMII at the cellular scale (Figure 1A; Supplemental Movie S1). NMY-2::GFP can be seen in foci distributed across the length of the cell in the cortical layer. These foci represent either individual NMII filaments, or small stacks of filaments—as observed by EM (Shutova *et al.*, 2014)—or one or more filaments that are too close to resolve by spinning-disk microscopy. We refer to these as NMII spots. The brightness of these spots and how densely packed they are per unit area of the cell change over space and time (Figure 1A). During the maintenance phase, NMII spots are brighter and more densely packed at the anterior side and dimmer and less densely packed at the posterior side. During ring assembly, the density and brightness of NMII spots decrease at the anterior side and NMII spots are enriched at the equator. During construction of the ring, the signal from NMY-2::GFP at both poles is low and the NMY-2::GFP signal disappears as the cortex is pulled out of the imaging plane as the cytokinetic ring ingresses (Figure 1A). These observations are consistent with previous work (Munro *et al.*, 2004; Maddox *et al.*, 2007; Kumfer *et al.*, 2010; Tse *et al.*, 2011, Li and Munro, 2021). We then considered the behavior of NMII at the scale of individual NMII spots. We observed examples of filaments being recruited to the cortex and increasing in apparent brightness. Figure 1B shows an example of an empty patch of actin where NMII spots seem to bind (arrowheads) with one prominently increasing in brightness (arrow). Also, we observed cases of spots unbinding from the cortex (i.e., disappearing from one frame to the next; Figure 1B). We also observed NMII spots dividing; for example, one spot moves along an actin filament then splits into two spots (Figure 1B, arrowheads) which move apart along the direction of the actin filament (Figure 1B, magenta arrow). From this we conclude that the rearrangement of the cortex from the anterior to the equator might arise from the dynamics of NMII.

sections are shown for each time point (zoom): one in the anterior and one in the equator where the ring will form (white dashed boxes). Scale bar: 10 μm; time is relative to the start of the assembly of the ring; A, anterior pole of the cell; P, posterior pole; inset, zoom. (B) Representative examples of NMII spots binding, dividing, and unbinding (scale bar, approximately 1 μm; time interval, 5 s. (D–G) Myosin density and intensity was plotted for the maintenance phase (blue), the start of ring assembly (dark green), the late ring assembly (light green), and the ring constriction (orange) for 10 spacial bins along the AP axis. The total NMII fluorescence intensity for the whole bin (D), the fluorescent intensity for segmented NMII spots (E), the number of NMII spots per unit of area of the cortex (F), and the spot intensity multiplied by the density (G) are plotted separately. Error bars: mean ± SD.

To understand how the dynamics of NMII might change over space and time, we quantified the total intensity of NMY-2::GFP for 10 spatial bins along the AP axis (Figure 1D) in accordance with previous work (Mayer *et al.*, 2010; Reymann *et al.*, 2016). These data show a peak in the anterior bins and lower values at the posterior side during the maintenance phase. This peak shifts to the equator during assembly and constriction (Figure 1D). A net increase of NMII at the cortex could be driven by an increase in the number of NMII motors per NMII filament, an increase in the number of filaments at the cortex, or both. Therefore, if NMII motors are recruited to NMII filaments that are already bound to the cortex, then an increase of NMY-2::GFP intensity in individual NMII spots should be seen. Alternatively, if new filaments are recruited to the cortex then an increase in NMII spot density should be observed. To discriminate between these possibilities, we tracked individual NMII spots using the Mosaic Particle Tracker (Sbalzarini and Koumoutsakos, 2005) and extracted qualitative data about their number per unit area and their brightness (Supplemental Figure S1; *Materials and Methods*). With these data, we measured two parameters: spot density—the number of spots per unit area (counts/μm^2)—and spot intensity—the number of NMII molecules per NMII filament as quantified by the fluorescence intensity of NMY-2::GFP signal per spot. Plotting these values along the AP axis showed that NMII redistributes from the anterior side of the embryo during the maintenance phase to the posterior side as the ring assembles (Figure 1, E and F). We multiplied the spot densities by the mean spot intensity for each bin (Figure 1G) which, at all four time points analyzed, gives rise to a distribution that resembles the original NMII intensity profile shown in Figure 1D. Diffusely localized NMY-2::GFP molecules in the cortical plane, which are not incorporated into NMII filaments, and out of focus light would contribute to the total fluorescence but not the density and intensity measurements in segmented tracks. Therefore, measuring the intensity and density of tracked NMII spots provides a more accurate estimate of the NMII that contributes to force generation. We conclude that the assembly of the cytokinetic ring is accompanied by both an increase of the number of NMII motors per NMII filament and an increase of NMII filament density in the cortex.

NMII filament density and intensity increase during assembly of the ring

We next looked in more detail at how NMII filament characteristics change with time. To do this, we looked with higher temporal resolution at the NMII spot density and intensity. The time when myosin intensities started to increase at the equator was used to temporally align the dataset (*Materials and Methods*). Regions were drawn in the anterior and posterior sides of the cell and the average density and intensity of NMII spots in these two regions of interest (ROIs) were plotted over time (Figure 2). During the maintenance phase (–200 to 0 s), both NMII spot density and intensity are relatively low in the posterior where the contractile ring forms. Then, NMII spot density and intensity rapidly increase over a period of about 50 s after the assembly of the ring starts. Thereafter, intensity and density measurements drop off due to the ingression of the cytokinetic ring pulling the cortex out of the imaging plane. In contrast, both these parameters are relatively high at the anterior during the maintenance phase. Thereafter, they remain constant for the first 50 s after the ring starts to assemble and then drop relatively slowly at around 50–100 s after the ring assembles, reaching lower values 2–3 min after the onset of the assembly of the ring (Figure 2). These changes in NMII spot density and intensity are consistent with the recruitment of NMII filaments and motors to the equator as the contractile

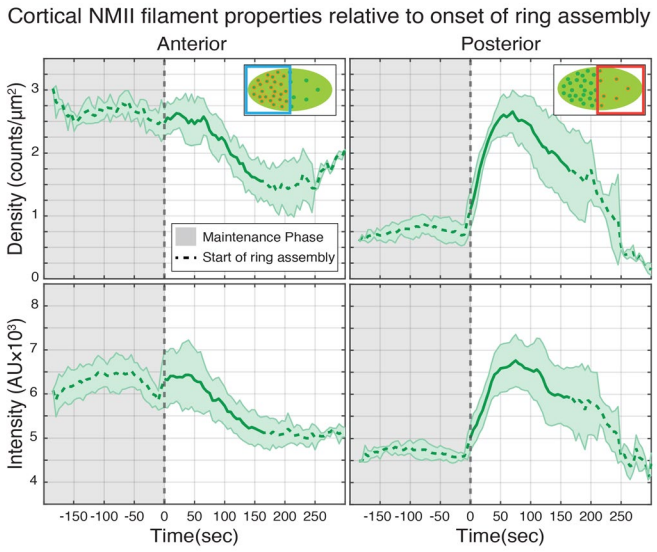

FIGURE 2: NMII density and intensity increase at the posterior and decrease in the anterior during ring formation. The NMII spot density per μm^2 of the cortex is plotted over time for regions in the anterior and posterior (insets). NMII spot fluorescence intensity is plotted in the same way. Time is relative to the start of the assembly of the ring; t = –200-0 covers the end of maintenance phase; the vertical dashed line is the start of ring assembly; t = 0-200 covers ring assembly and constriction. The line and shaded area, mean of seven embryos ± SD; dotted line, average of 6 or less repeats.

ring forms and the disassembly of the anterior cap shortly thereafter. To conclude, we observe a rapid increase in both NMII filament density and intensity at the posterior during the transition from maintenance to ring assembly.

Superresolution imaging of NMII dynamics in the cortex

To better resolve the NMII filament behaviors that were observed with spinning-disk microscopy, we imaged NMII at higher spatial resolution using structured illumination total internal reflection fluorescence imaging (SI TIRF; Guo *et al.*, 2018). We observed the same disassembly of cortical NMII in the anterior and a concomitant assembly of the cytokinetic ring (Figure 3A; Supplemental Movie S2) as we had seen with the spinning-disk imaging modality. We also imaged at higher temporal resolution and could again see NMII spots binding, unbinding, and dividing (Figure 3B). However, at this higher resolution we could be more confident that division events were not in fact two overlapping NMII filaments but rather individual filaments splitting (Fenix *et al.*, 2016; Beach *et al.*, 2017). Individual NMII filaments were segmented and tracked as before (Supplemental Figure S1). The intensity profiles for individual filaments in the anterior and posterior are plotted as color-coded tracks (Figure 3C). The tracks are stacked in the order in which they appeared in the cortex, and each track starts at the time at which the corresponding filament first appeared. This visualizes both the rate of NMII filament recruitment (Figure 3C, white lines) and the time course of filament assembly dynamics. The general trend is that filaments are first recruited to the cortex and then increase in intensity to a peak followed by a decrease in intensity before being lost from the cortex. This is illustrated by the tendency of tracks to become brighter—more yellow and white pixels—with time (Figure 3C and Supplemental Figure S2, A and B). In the anterior, new NMII filaments are recruited to the cortex with a decreasing rate over time. Tracks are also brighter and longer in the maintenance phase and shorter and

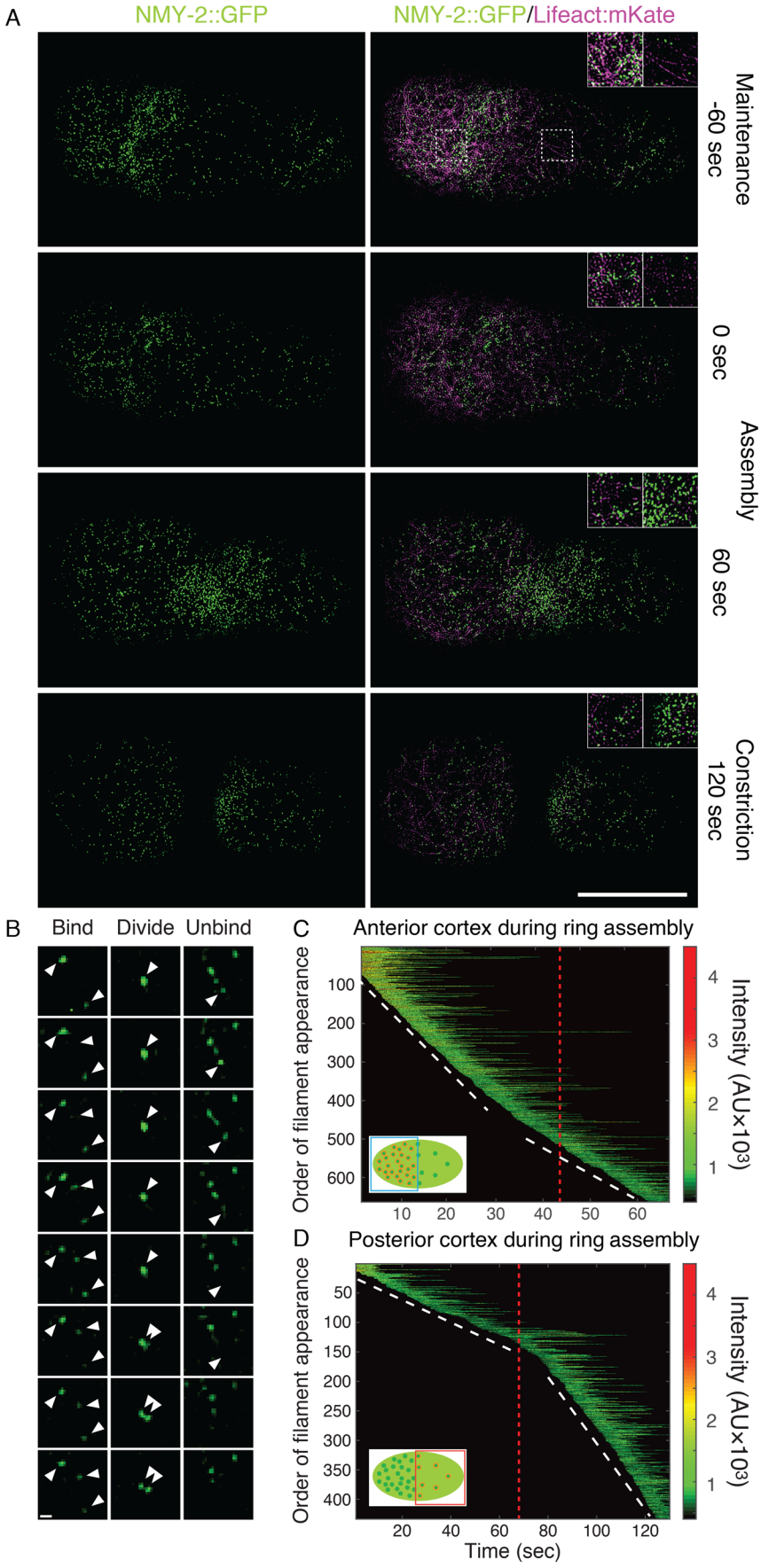

dimmer during ring formation (Figure 3C; Supplemental Figure S2, A and B). The opposite is true in the posterior where the rate of NMII filament recruitment suddenly increases at the onset of the ring formation (Figure 3D, red line) and there is a trend for tracks to be longer and have higher intensities after ring formation compared with those during the maintenance phase. We quantified the intensity changes in more detail (see Supplemental Data). In the anterior during maintenance, NMII filaments typically first grow in intensity before they drop below their starting intensity after approximately 10 s. In contrast, filaments appearing in the posterior during ring assembly increase to a higher brightness and stay bound for longer (Supplemental Figure S2, C and F). These data are consistent with NMII filaments disassembling from the anterior and assembling at the posterior as the ring forms. More strikingly, the sudden increase in the rate of NMII filament recruitment at the equator around the time of the onset of the formation of the cytokinetic ring indicates that there is a regulatory switch that activates ring assembly, likely via local RHO-1 activation (Tse *et al.*, 2012). This regulation seems

FIGURE 3: Superresolution imaging of NMII filaments in the cortex and show dynamics at the cortex and a sharp increase in the recruitment rate as the ring assembles. (A) Superresolution SI TIRF microscopy images of *C. elegans* one-cell labeled with NMY-2::GFP (green) and the marker for actin filaments, LifeAct::mKate (magenta). Representative images of cells during the maintenance phase ($t = -60$ s), assembly of the ring ($t = 0$-60 s) and during cytokinesis are shown (t = 120 s). Two enlarged sections are shown for each time point (insets): one in the anterior and one in the equator where the ring will form (white dashed boxes). Scale bar: 20 μm; time is relative to the start of the assembly of the ring. A, anterior pole of the cell; P, posterior pole. (B) Representative examples of NMII filaments binding to the cortex, dividing and unbinding (scale bar: 5 pixels or approximately 0.200 μm; time interval: 90 ms). (C) Color-coded tracks were plotted for individual tracked NMII filaments in the anterior and equator (insets). Each track starts at a position on the *x*-axis that corresponds to the time when a filament appeared at the cortex. The color of each track corresponds to the intensity of the filament (black, low intensity; green-yellow, higher intensities). These intensity profiles were then stacked on the *y*-axis in the order in which the corresponding filament appeared at the cortex (top first, bottom last) and a vertical red line shows the time when the ring starts to assemble. The top tracts represent the filaments that are in the field of view at the start of the movie. The white dashed lines are a guide to the eye for the rate of NMII filamnet recruitment to the cortex (arrival events per unit of time).

to act by increasing the recruitment of new NMII filaments to the cortex and also the recruitment of new NMII motors to pre-existing NMII filaments.

Key myosin regulators modulate both NMII spots density and intensity

To test what might regulate the increase in NMII filament density and intensity at the cortex as the ring assembles, we chose two candidate proteins that are known to influence NMII activity (Figure 4A). These proteins were LET-502 and MEL-11. LET-502 is the *C. elegans* Rho1-dependent kinase which activates NMII activity by phosphorylating its regulators light chain, MLC-4 (Piekny *et al.*, 2003). MEL-11 is the *C. elegans* myosin phosphatase-targeting subunit that inhibits NMII activity by dephosphorylating MLC-4 (Piekny and Mains, 2002; Piekny *et al.*, 2003). To test the role of these two proteins in regulating NMII during ring assembly, we performed RNA interference (RNAi) of *let-502* and *mel-11* and then performed time-lapse imaging of *C. elegans* embryos expressing NMY-2::GFP and Lifeact::mKate.

For *let-502* RNAi, imaging revealed phenotypes that confirmed the RNAi was effective after 28–29.5 h of knockdown (Supplemental Data). For example, the anterior cap is larger than that in wild type (Figure 4B), and particle image velocimetry (PIV) analysis of NMII during the early flow phase shows a decrease in NMII velocity along the AP axis (v_x) compared with wild type (Figure 4C). We then measured the changes in NMII spot density and intensity over time, as previously done for wild type. When LET-502 is depleted, the density and intensity of NMII spots during the maintenance phase (t = –200–0 s) in the posterior are higher than in wild type (Figure 4D). The higher NMII values are likely due to the lower flow velocity in *let-502* RNA (Figure 4C). Lower flow velocities would compress the cortex less resulting in a larger anterior cap. This larger cap would then overlap with the posterior where the ring forms (Figure 4B). NMII in the anterior cap is first cleared from where it overlaps with the posterior half of the cell before the ring assembles (Figure 4D; *Materials and Methods*). At the anterior side of the cell during the end of the maintenance phase, the drop in NMII spot density starts about 100 s earlier than in wild type. Later on, LET-502 depletion reduces NMII spot density and intensity in the ring (Figure 4D). These observations are consistent with the known role of LET-502 as an activator of NMII activity via phosphorylation of MLC-4 (Piekny and Mains, 2002) and its role downstream of RHO-1 (Green *et al.*, 2012). To conclude, these data suggest that the specific function of LET-502 is to keep NMII filament density high in the anterior cap during the maintenance phase—alongside CDC-42 (Schonegg and Hyman 2006)—and then to recruit new NMII filaments at the equator during the assembly of the ring and to assemble more NMII motors to them.

For *mel-11* RNAi, imaging also revealed phenotypes that confirmed that the RNAi was effective after 25–29.5 h of knockdown (Supplemental Data). For example, there was a shorter actomyosin-rich anterior cap during the maintenance phase (Figure 4B) and PIV analysis of the flow phase indicated an increase in v_x (Figure 4C). This is consistent with the known role of MEL-11 as a repressor of myosin activity (Piekny and Mains, 2002). We then measured the changes in NMII spot density and intensity over time, as previously done for wild type. This showed no large changes in NMII spot density and a drop in NMII spot intensity in the posterior compared with wild type (Figure 4D). Paradoxically, this decrease was similar to the *let-502* phenotype, although not to the same extent. This result is not consistent with the expected role of MEL-11 as a negative regulator where an increase in NMII recruitment would be expected to lead to an increase in myosin density compared with wild type. We hypothesized that this might be a consequence of a loss of MEL-11 activity during the flow phase which then indirectly affects the assembly of the ring by interfering with the dynamics of NMII disassembly in other regions.

A pool of free NMII in the cytoplasm

To investigate this hypothesis, we applied the following logic: *let-502* and *mel-11* RNAi might influence the amount of NMII at the future site of division due to the way NMII moves from the anterior cap to the equator. NMII might be released from the anterior cap into the cytoplasm where it might form a pool of free motors that then assemble into the cytokinetic ring. To test if this was the case, we examined images of the cytoplasm at a depth of 10 µm below the cortical plane, approximately in the middle of the cell. These images were acquired simultaneously with the images of the cortex used in previous analyses. These images show that there is a GFP signal in the cytoplasm that is brighter than the background signal outside of the cell (Figure 5 and Supplemental Figure S4). Small NMII spots are also visible in the cytoplasm (Figure 5A and Supplemental Figure S4, arrowheads) that has a similar size and brightness to those in the cortex (arrows), which can be seen at the periphery of the cell. We conclude that the cytoplasmic signal consists of two populations of molecules: 1) uniformly localized NMII that, most likely, consists of freely diffusing NMII motors and 2) NMII spots that are likely filaments that are either free in the cytoplasm or transiently bound to actin or other cytoplasmic structures (Supplemental Data).

A cytoplasmic pool of free motors is the source of NMII for the cytokinetic ring

We hypothesized that there might be an exchange of NMII between the cortex and the cytoplasm because of the following observations. The decrease in the NMY-2::GFP intensity and density in the anterior only occurs at about 50 s after the start of ring assembly. This is about 50 s before we observed an increase in NMII density and intensity in the posterior (Figure 2). If the NMII that is assembled into the ring does not come from the anterior cap then it might come from the cytoplasm. We set about to test this hypothesis by looking in more detail at the cytoplasmic pool of NMII. We first quantified the total amount of NMII in the cytoplasm. To do this, we measured the total fluorescence intensity of NMY-2::GFP in a rectangular region in the cytoplasm of images of the midplane, avoiding the periphery of the cell where the signal from the cortex perpendicular to the imaging plane can be seen (Figure 5B, inset). To counteract large embryo-to-embryo variability, the intensity values were normalized relative to the value at t = 0, meaning that the graphs represent a fold change in intensity relative to that time. This showed that the total NMY-2::GFP intensity is relatively high and varies only slightly for the 200 s before the onset of ring assembly (Figure 5B and Supplemental Data). Then, the cytoplasmic NMY-2::GFP intensity falls steeply during the 50 s after the onset of the assembly of the ring and thereafter remains low (Figure 5B). This represents the time during which there is a large increase in NMII spot density and intensity in the cortical plane at the equator (Figure 2). In conclusion, the precise timing of the decrease in NMII in the cytoplasmic pool simultaneously with the increase in NMII in the cortex (Figure 2), indicates that the NMII needed to build the ring comes from the free pool of motors in the cytoplasm.

To quantify the number of NMII spots in the cytoplasm, we segmented the images and counted the number of spots per unit area. To do this, we used the Ilastik image segmentation algorithm (Berg *et al.*, 2019) which was trained to identify spots in the cytoplasm but

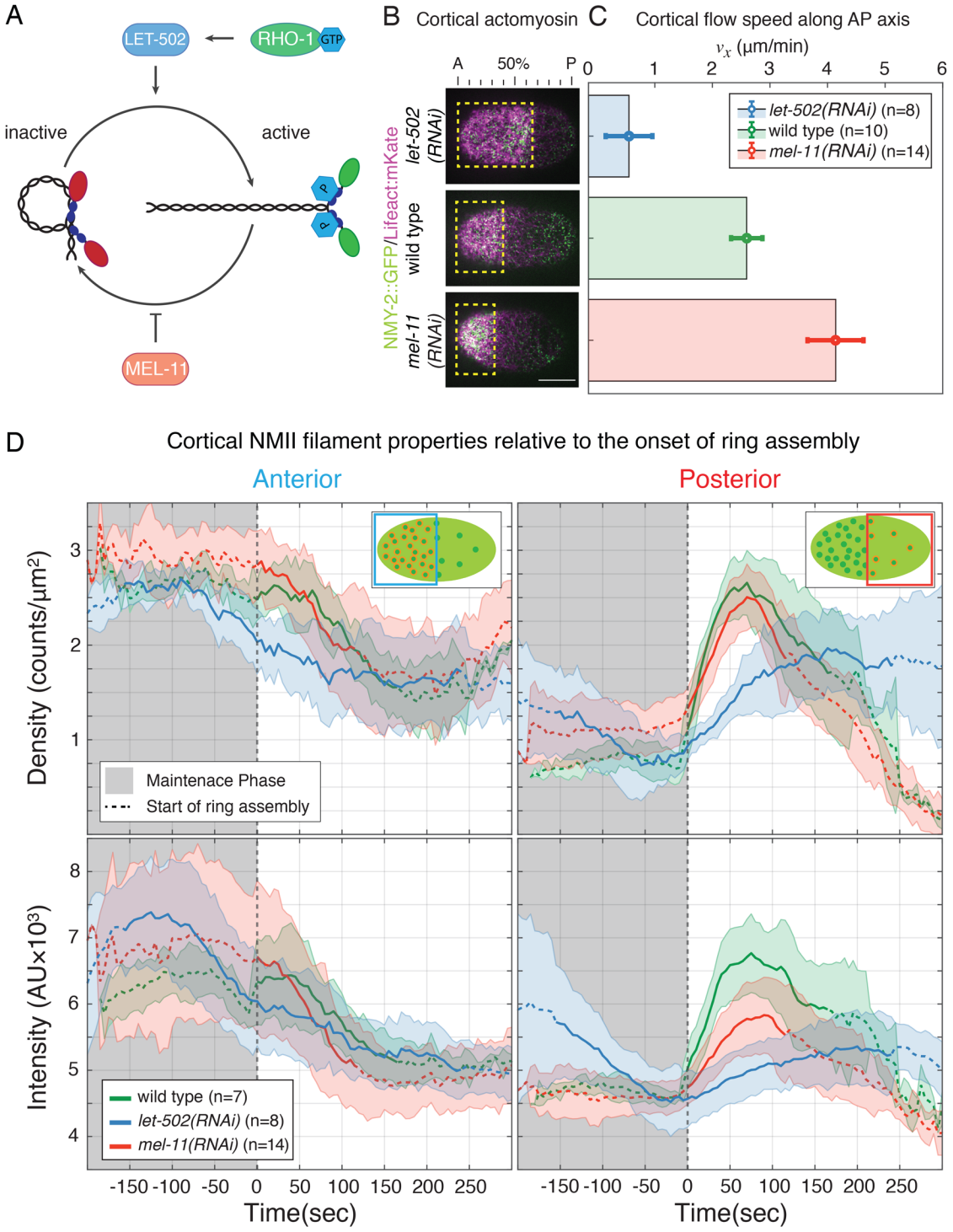

FIGURE 4: Regulators of NMII activity affect the cortical dynamics and the assembly of the ring. (A) Scheme of the function of LET-502 and MEL-11. MEL-502 is activated by RHO-1 which in turn activates NMII by phosphorylating its RLC MLC-4 (purple circle). This converts inactive NMII (red) to the active conformation (green). MEL-11 deactivates NMII by removing the phosphate on MLC-4 and returning NMII to its inactive conformation. (B) microscopy images of cells during the maintenance phase subjected to RNAi against *let-502* and *mel-11*. The localization of NMY-2::GFP (green) and LifeAct::mKate (magenta) is shown for the two RNAi conditions and wild type. Scale bar: 10 µm; yellow box, the size of the anterior cap. (C) PIV quantifying the flow of the cortex along the AP axis (V_x) in the posterior for the three conditions. Error bars: mean ± SD. (D) The NMII spot density per µm^2 of the cortex is plotted over time for regions in the anterior and posterior (insets) for *let-502* RNAi (blue) and *mel-11* RNAi (red) compared with wild type (green). NMII spot fluorescence intensity is plotted in the same way. Time is relative to the start of the assembly of the ring; line and shaded area, mean ± SD; dotted line, average for time points which were not covered by all repeats.

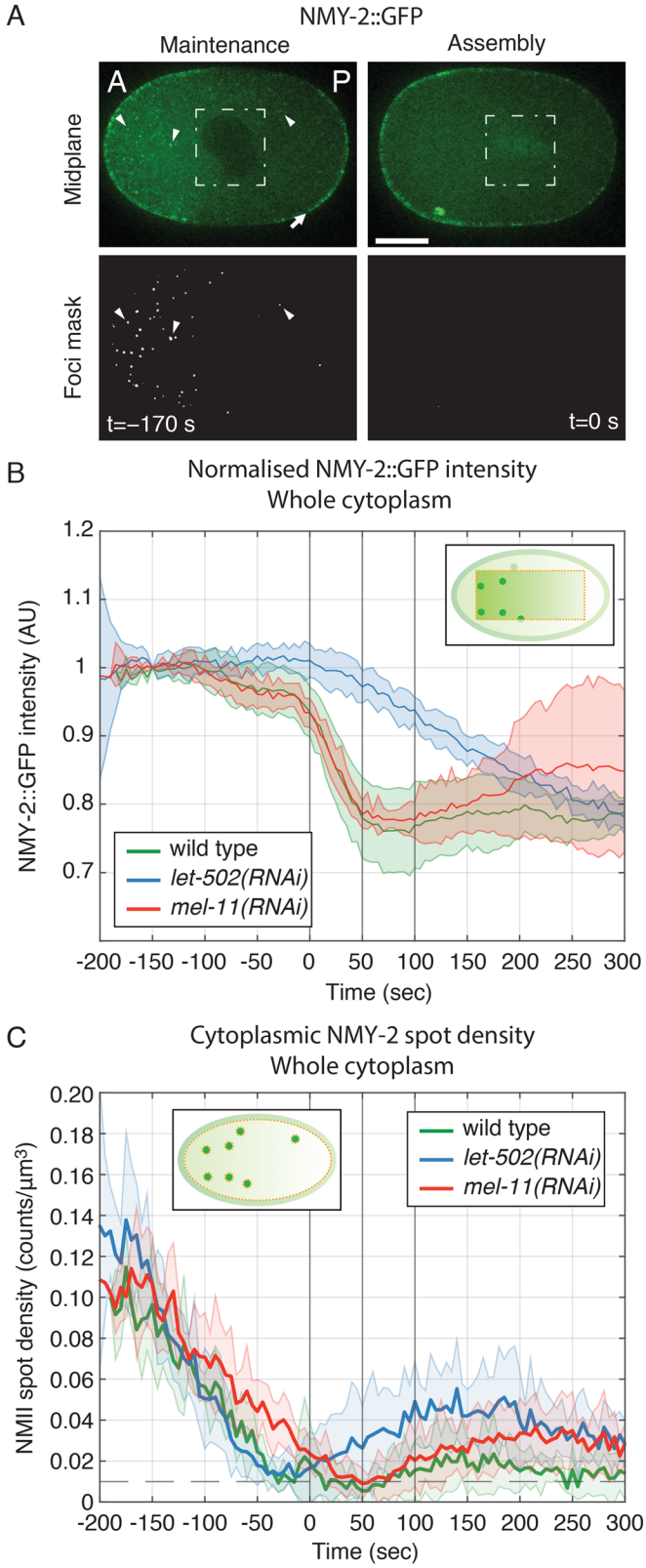

FIGURE 5: Quantification NMY-2::GFP reveals changes in NMII concentration around the time the ring assembles that is affected by RNAi of *let-502*. (A) Spinning-disk microscopy images of NMY-2::GFP of the midplane of one-cell *C. elegans* embryos during the maintenance phase and during assembly of the cytokinetic ring. Dashed white boxes show where the NMY-2::GFP signal is excluded from the pronucleus (maintenance phase) and enriched in the spindle (assembly of the ring). The output of the segmentation of cytoplasmic is show which robustly identifies cytoplasmic NMII spots (arrowheads) and can distinguish them from cortical NMII in the plane perpendicular to the imaging plane (arrows). Scale bar: 5 μm; time is relative to the start of the assembly of the ring as judged for the cortical plane; A, anterior pole of the cell; P, posterior pole. (B) The average pixel intensity for cytoplasmic NMY-2::GFP at midplane plotted over time for wild type (green), *let-502* RNAi (blue), and *mel-11* RNAi (red). The data are for a rectangular ROI covering the whole AP axis but excluding the cell periphery (inset). Intensity values are normalized such that the intensity during the maintenance phase ($t = -150$) is 1, meaning that the data represent the relative change in NMY-2::GFP intensity over time. (C) The NMII spot density per unit volume of the whole cytoplasm plotted over time calculated from the spot mask. Dashed line, 0.01 counts/μm³.

to exclude the cortical NMY-2::GFP signal (Figure 5A). We then counted the number of NMII spots per unit area of an image and converted this to a volume assuming a thickness the optical section of ~0.56 μm (*Materials and Methods*). As before, these measurements were made for the period between the end of maintenance phase and the assembly of the ring (Figure 5C). These data show that the number of cytoplasmic NMII spots is 0.1 counts/μm^3 at 200 s before the assemble of the ring. The number of NMII spots then drops until it reaches approximately 0.01 counts/μm^3 about 30 s before the ring starts to assemble (Figure 5C). This suggests that NMII filaments in the cytoplasm disassemble into free NMII motors or binding back to the cortex as the cell cycle continues. As we observe a low number of NMII spots, we conclude that this does not provide a significant source of NMY-2 for the ring.

Cytoplasmic NMII forms an anteroposterior gradient

Having shown that there are temporal changes in cytoplasmic NMII, we wanted to know if there are also spatial changes in NMII. Indeed, the images of the midplane show that the cytoplasmic NMY-2::GFP signal and the number of NMII spots in the cytoplasm seemed to be higher at the anterior (Figure 5A and Supplemental Figure S5). To quantify this, we measured the intensity of NMY-2::GFP in the cytoplasm along the AP axis. To do this, we divided the cytoplasm into 18 bins along the AP axis and masked out the cortex at the periphery of the cell and the part of the cytoplasm where the spindle forms (Figure 5A). We measured the absolute values of NMY-2::GFP signal per unit area for a time point 60 s before the onset of ring assembly, a time when cortical concentrations of NMII are stable. This showed that there is a cytoplasmic gradient with the highest NMII concentration at the posterior edge of the anterior cap and (in bin five), consistent with previous observations of this enrichment driven by cortical flows (Munro *et al.*, 2004). NMII concentrations then dropped before reaching a trough at the 17th bin (Figure 6A). The response of the cytoplasmic NMY-2::GFP concentration has a complex spatial pattern that could be fitted with a fourth-order polynomial. Plotting the tangent of the fit at the inflection point between the peek and trough gives a reasonable estimate of the slope (Figure 6A). This gradient is most likely established because higher concentrations of NMII at the anterior cap mean more motors are released into the cytoplasm at the anterior side. To test if the dynamics of actomyosin affected the cytoplasmic gradient, we interfered with actin polymerisation with the drug Latrunculin A and looked for changes in the localisation of NMII in the cytoplasm. The drug treatment lead to the disassembly of the anterior cap and abolished the cytoplasmic NMII gradient (Supplemental Figure S6

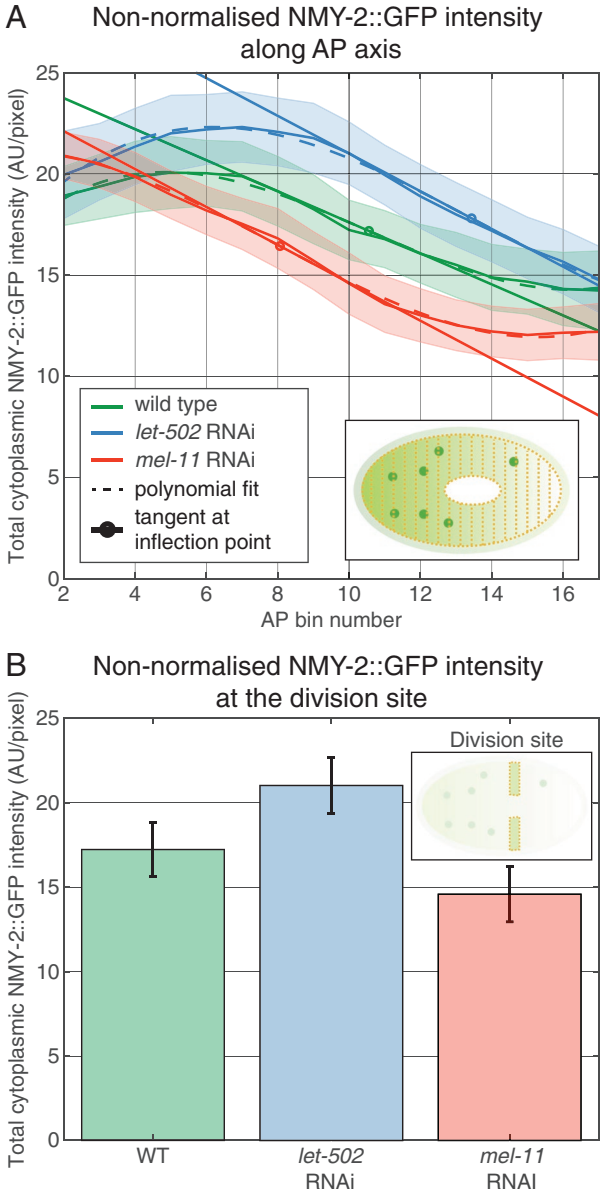

FIGURE 6: The gradient and NMII concentrations in the cytoplasm are affected by RNAi of *let-502* and *mel-11*. (A) Nonnormalized pixel intensity values for NMY-2::GFP in the cytoplasm for 18 spatial bins along the AP axis (inset) for the time point 60 s before the onset of ring assembly. The values are for the total pixel intensities including the diffuse signal and the spots (inset). The mean and SD of the data are plotted for wild type in green (solid line, mean; shaded area, ± SD), *let-502* RNAi in blue and *mel-11* RNAi in red. Each dataset was fitted with a fourth-order plolynomial (dashed line), and the gradient was measured by calculating the gradient at the point of inflection (open circle). (B) Bar chart of the NMY-2::GFP intensity at the site of the future division plane (corresponding to bin 10 in panel A).

and Supplemental Data) establishing a link between the cortical and cytoplasmic NMII gradients.

Regulation of NMII activity via Rho signaling mediates exchange of myosin between cortex and cytoplasm

If the levels of NMII in the cortex are regulated by LET-502 and MEL-11 and there is exchange between cortical and cytoplasmic pools of NMII, then one would expect these two regulators also to affect the dynamics of NMII in the cytoplasm. We hypothesized that exchange between these two pools of NMII might explain changes in the cytoplasmic NMII and could explain the unexpected results where *mel-11* RNAi resulted in a drop in NMII recruitment during ring assembly despite it being a negative regulator of NMII activity (Figure 4D). To test if this was the case, we analyzed the cytoplasmic NMY-2::GFP intensities in embryos subject to RNAi of these two regulators (Figure 5, B and C). The RNAi of *mel-11* did not affect the drop in cytoplasmic NMY-2::GFP intensity during assembly of the ring (Figure 5B). In contrast, RNAi of *let-502* shows a much slower drop in the cytoplasmic intensity reaching low levels only after about 250 s after ring assembly starts compared with 20 s in wild type (Figure 5B). This shows that LET-502, alongside being required for the increase in cortical NMII at the equator, is also required for the concomitant drop in NMII in the cytoplasm. From this we propose that LET-502 is active during assembly of the cytoplasmic ring, consistent with its general role as an activator of NMII (Piekny and Mains, 2002). Next, we looked at the NMII spot density in the cytoplasm for the two RNAi conditions. For *let-502* RNAi, the cytoplasmic density of NMII spots is similar to that of wild type (Figure 5C). In contrast, the drop in the NMII spot density is delayed in *mel-11* RNAi compared with wild type, reaching 5×10^{-3} at around 50 s after the assembly of the ring starts, representing a delay of approximately 80 s (Figure 5C). We propose that MEL-11 also acts around the time of ring assembly to deactivate cytoplasmic NMII filaments and release free NMII motors into the cytoplasmic pool, consistent with its general role as inhibitor of NMII (Piekny and Mains, 2002).

If LET-502 does predominantly act to assemble NMII filaments at the ring and MEL-11 to release free NMII motors, then we would expect RNAi of these two regulators to affect the cytoplasmic gradient of NMY-2. To test if this was the case, we again plotted the raw, nonnormalized NMY-2::GFP intensity values. We plotted NMY-2::GFP intensities along the AP axis 60 s before the onset of ring assembly for the two RNAi conditions. The data plotted in this manner allow the comparison of raw intensity values between RNAi conditions and wild type. The two RNAi treatments affect the pattern of cytoplasmic NMY-2::GFP concentration. When MEL-11 and LET-502 are depleted, the distributions of cytoplasmic NMII are shifted toward the anterior and posterior, respectively (Figure 6A). These effects are likely due to the changes in cortical flow speed during the flow phase (Figure 4C). More significantly, the general trend for the NMY-2::GFP concentration is that fluorescence intensity values are lower in the absence of MEL-11 and higher in the absence of LET-502. Evidence for this can be observed most clearly in bin 10 which is the position along the AP axis where the ring is about to form and therefore the point in the cytoplasm from which motors will be recruited into the ring. Here the NMY-2::GFP intensity is significantly lower when *mel-11* is subject to RNAi and significantly higher for *let-502* compared with wild type ($p = 0.0011$ and $p = 0.0138$, respectively; Figure 6B). From this we conclude that the role of LET-502 is to keep NMII motors in the active state and bound to the cortex thereby keeping cytoplasmic concentrations low. When LET-502 is depleted, less NMII motors enter the cytoplasmic pool which increases concentrations locally which in turn affect global concentrations via diffusive flux. Similarly, the role of MEL-11 is to deactivate NMII motors and remove them from the cortex thereby keeping cytoplasmic concentrations high. When MEL-11 is depleted by RNAi, more motors remain bound to the cortex and which lowers the cytoplasmic concentration. This result also explains the observation that, despite being a negative regulator of NMII activity, MEL-11 depletion slows down the recruitment of NMII to the ring. This is because the lower cytoplasmic NMII concentration seen in

mel-11(RNAi) would decrease the rate that NMII binds to the cortex at the site of the ring. In summary, data on how LET-502 and MEL-11 affect the dynamics of NMII suggest that the role of these two regulators is to act in a coordinated way to fine-tune the gradient of NMII in the cytoplasm down which NMII motors might move via diffusive flux to the sight of the cytokinetic ring.

DISCUSSION

High-resolution imaging of the cortex showed individual spots of NMII binding to the cortex, growing in brightness, and unbinding from the cortex of the *C. elegans* one-cell embryo. Quantification of the density of these NMII spots and their intensity indicate that new NMII filaments form at the cortex during the assembly of the cytokinetic ring, and that pre-existing NMII filaments that are already bound to the cortex grow by the addition of additional NMII heterohexamers. These dynamics are consistent with the mode of activation of NMII by phosphorylation of its RLC downstream of RhoA/RHO-1 as already shown (Lecuit *et al.*, 2011; Tse *et al.*, 2012). Such dynamics have previously been observed in the lamellar of cultured cells using superresolution microscopy (Beach *et al.*, 2017). We also observe NMII filaments dividing. This offers the cell another mechanism to increase the number of filaments in the cortex. The division, or partitioning of NMII filaments, has been seen in the cortex of cultured cells and may happen because of steric hindrance between NMII heads in large filaments by templated nucleation or because higher pulling forces in larger NMII filaments pull filaments apart (Fenix *et al.*, 2016; Beach *et al.*, 2017; Burnette *et al.*, 2020). The latter might be the favored mechanism in the *C. elegans* cortex because we observe spots moving apart along filaments of actin. These three factors (NMII filament recruitment, growth, and division) increase the total amount of NMII in the cortex which, in turn, increases cortical tension and ultimately generates the force to constrict the membrane.

The increase in both the number of NMII filaments bound to the cortex and the number of NMII motors in each filament represents two ways the cell can control the behavior of the cortex, given that NMII filaments can act both as a cross-linker and as a motor protein (Maddox *et al.*, 2007; Ding *et al.*, 2017; Descovich *et al.*, 2018). First, increasing the number of filaments bound to the cortex increases the level of cross-linking between actin filaments. Second, changing the number of NMII motors per filament increases the pulling forces it can exert on the actin network. The biochemical activation of NMII offers a possible explanation for the mechanism behind the concomitant increase in the number and size of NMII filaments (Fenix *et al.*, 2016). A proportional increase of NMII filament number and size might be governed by the common mode of NMII activation downstream of RHO-1 (Lecuit *et al.*, 2011; Tse *et al.*, 2012). The increase in number and size of NMII filaments would be relevant for the function of the actomyosin cortex in the cell because it would change the physical properties of the cortex by modulating its tension, stiffness, or viscoelastic properties (Salbreux *et al.*, 2012). If NMII filament size increased while their density remained low, the resulting increased cortical tension due to higher motor activity might lead to cortical tearing (Chanet *et al.*, 2017). In contrast, if NMII filament density increases while their size remained low, then the cortex would be more cross-linked and therefore become too stiff to constrict (Maddox *et al.*, 2007; Ding *et al.*, 2017; Descovich *et al.*, 2018). Therefore, our data suggest that the cell tunes the increase in NMII filament density and intensity such that the force generated can be effectively propagated through the cortex to ensure successful furrow ingression (Alvarado *et al.*, 2013). Further work is needed to validate this mode of action in *C. elegans* and our quantitative data would be valuable for theoretical models of how such forces generated at the cortex could lead to smooth ingression.

The sharp increase in NMII filament density and intensity as the ring starts to assemble indicates that this process is regulated. We show that two proteins in the RhoA/RHO-1 pathway influence this process consistent with their known role in regulating NMII (Piekny and Mains, 2002; Maddox *et al.*, 2007; Kumfer *et al.*, 2010; Lewellyn *et al.*, 2018). These two proteins are the *C. elegans* orthologs of the Rho-dependent kinase, LET-502, and the myosin phosphatase, MEL-11 (Wissmann *et al.*, 1997; Piekny *et al.*, 2003). LET-502 and MEL-11 likely function together with other factors known to influence the cortex in the one-cell embryo, namely, another Rho family member, CDC-42 (Dechant and Glotzer, 2003; Kumfer *et al.*, 2010). We show that LET-502, an activating kinase, positively regulates the speed of the cortex during the flow phase (Nishikawa *et al.*, 2017). In contrast, MEL-11, an inhibitory phosphatase, negatively regulates the speed of the cortex during the flow phase. Together, these two regulators fine-tune the distribution of NMII in the anterior cap during the maintenance phase. This then indirectly influences the assembly of the ring via the cytoplasmic pool of NMII motors (as discussed below). Additionally, these two regulators act during the period between the end of maintenance phase and the start of ring assembly; MEL-11 is required to deactivate NMII motors at the anterior cap causing NMII filaments to unbind from the cortex and disassemble to release NMII motors into the cytoplasm. As the ring assembles, LET-502 is required to activate NMII, recruiting NMII motors to the cortex at the equator to build the cytokinetic ring.

A key result of our work is the observation and quantification of a pool of free NMII in the cytoplasm. Models of this behavior have previously been proposed by Beach *et al.* (2017) who observed NMII assembly in tissue culture cells at superresolution and concluded that activation of NMII assembly in different compartments (lamellar cortex and stress fibers) of the cell competes for a pool of free NMII. We confirm that this is the case and build on this by directly imaging and quantifying the pool, which is possible in *C. elegans* due to the separation of compartments we image compared with the crowded cytoplasm of fibroblast lamella (Beach *et al.*, 2017). In the case of *C. elegans*, this pool consists of NMII filaments that have likely been released from the anterior cortex which then disassemble into NMII motors, as well as motors that are released from NMII filaments still bound to the cortex. This is consistent with NMII being in dynamic exchange with NMII filament bound to the cortex (Fenix *et al.*, 2016; Gross *et al.*, 2018; Leite *et al.*, 2020). This pool is also dynamic and has a spatial pattern. The concentration of NMII in the cytoplasm is higher in the anterior and lower in the posterior and the global concentration of NMII in the cytoplasm decreases precisely as the ring assembles. This tight temporal correlation between the drop in cytoplasmic NMII concentration and the increase in cortical NMII concentration shows that this cytoplasmic pool is a source of NMII to make the cytokinetic ring. More interestingly, the cytoplasmic pool also acts as a path through which NMII motors can move presumably via diffusive flux down a concentration gradient as previously proposed (Billington *et al.*, 2013).

Combining our data with that from other labs leads us to present the following model for the behavior of the cortex (Figure 7). During the flow phase, cortical NMII flows from posterior to anterior and establishes the anterior cap (Piekny and Mains, 2002; Jenkins *et al.*, 2006; Pacquelet, 2017). During the maintenance phase, this level of NMII is kept high through the action of CDC-42 (Motegi and Sugimoto, 2006; Schonegg and Hyman, 2006; Kumfer *et al.*, 2010). The higher concentration of NMII at the

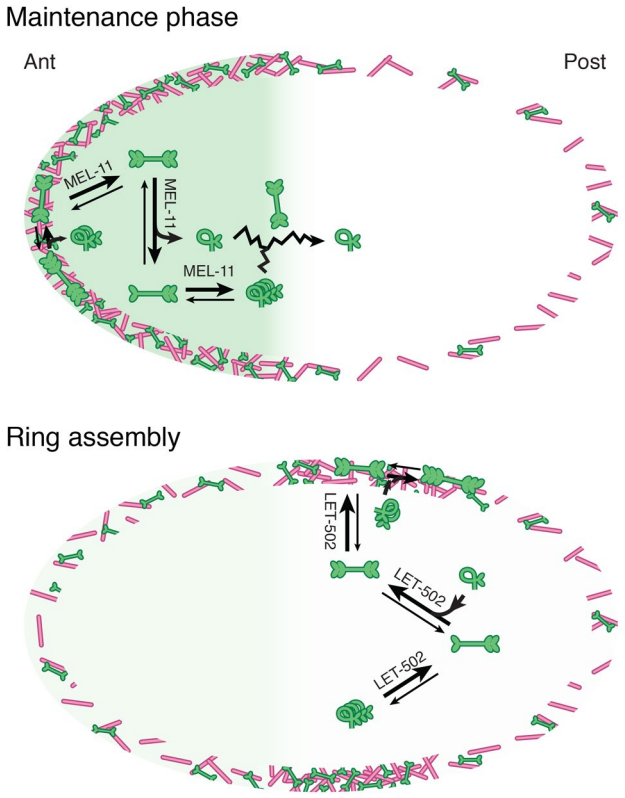

FIGURE 7: Scheme of cortical and cytoplasmic actomyosin in the one-cell *C. elegans* embryo. The distribution and assembly of actomyosin in the cortex and cytoplasm are represented during the maintenance phase and during ring assembly. Actin filaments are represented by pink rods and NMII are green sticks. The cytoplasmic concentration of NMII is represented by varying intensities of green. The arrows represent a dynamic exchange of NMII filament binding to and unbinding from the cortex. Cytoplasmic NMII becomes deactivated resulting in NMII filaments disassembling into free NMII motors (curly green sticks) which are then free to diffuse. We propose that MEL-11 promotes the disassembly of NMII at the anterior cap during the maintenance phase. This enriches NMII in the posterior half of the cytoplasm. In the posterior, the cortical concentration is low because of the movement of NMII to the anterior during flow phase, resulting in a lower off rate of NMII detaching from the cortex there. These two factors establish a cytoplasmic gradient of NMII that is high in the anterior and low in the posterior. Free motors in the cytoplasm can diffuse down the concentration gradient (zig-zag arrow) to the site of the future division plane. During ring assembly, LET-502 actives NMII, recruiting it to the ring thereby depleting motors from the cytoplasmic pool. Free motors assemble into filaments that bind to the cortex or are added to filaments that are already bound.

anterior cap increases the rate at which NMII leaves the cortex there, thereby establishing a cytoplasmic gradient of NMII. During ring assembly, the balance of NMII activation changes (Bringmann and Hyman, 2005; Wolfe *et al.*, 2009; Green *et al.*, 2012). At the anterior, MEL-11 activity dominates, deactivating NMII in the cortex at that side of the cell. This causes NMII motors to dissociate from NMII filaments and be released into the cytoplasm. NMII filaments are also released from the cortex into the cytoplasm where they then disassemble to release NMII motors. Cytoplasmic NMII then moves by diffusing down a NMII concentration gradient toward the future division plane. As RHO-1 activates ring assembly via LET-502, NMII is locally recruited from the cytoplasm at the equator, concomitantly depleting the cytoplasmic pool of free NMII. Recruitment of NMII from the cytoplasm to the cortex at the equator then leads to an increase in the number and size of NMII filaments at the site of the future division plane, which generates the force to ingress the cytokinetic ring (Figure 7). This shows that at the scale of the whole cell, the actomyosin cortex consists of spatially separated areas where NMII activity is differentially regulated, and that these areas communicate with each other via a freely diffusing pool of inactive motors in the cytoplasm (Billington *et al.*, 2013). We suggest that a similar mechanism might be in action in other cytoskeletal systems, for example, stress fibers in fibroblasts that have been shown to undergo turnover (Hu *et al.*, 2017) or in the lamella of HeLa cells where it has been proposed that NMII is recycled (Breckenridge *et al.*, 2009).

MATERIALS AND METHODS

Request a protocol through *Bio-protocol*.

Strains

C. elegans was propagated using standard methods (Brenner, 1974). Briefly, nematodes were cultured on OP50-seeded NGM plates at 20°C. For microscopy, animals were dissected in M9 buffer and then embryos were mounted between a pad of 2% agarose and a coverslip, a method known to compress the embryos slightly (Pimpale *et al.*, 2020). Imaging NMII and actin was performed using a dual-colored line called SWG007 expressing NMY-2 fused to GFP from its native promotor at its endogenous location (Dickinson *et al.*, 2013) and the actin binding protein Lifeact fused to mKate2 expressed from a germline-specific promoter at an ectopic locus (Reymann *et al.*, 2016): *nmy-2(cp8 [nmy-2::GFP unc-119+]) I; geaIs001 [Pmex-5::Lifeact::mKate2:: nmy-2UTR, unc-119+].*

RNAi knockdowns

Knockdowns were performed by feeding staged, L4 hermaphrodites with bacteria expressing the RNAi vector expressing the appropriate genomic fragments (Timmons *et al.*, 2001). Worms were grown on AGM agar plates containing 1 mM Isopropyl β-D-1-thiogalactopyranoside and 25 μg/ml carbenicillin seeded with bacterial clones from the Ahringer lab (supplied by Source Bioscience; Kamath and Ahringer, 2003). Nematodes were fed for 25–29.5 h for MEL-11depletion and 28–29.5 h for LET-502 depletion.

Latrunculin A treatment

The eggshells of early embryos were permeabilized with a *perm-1* (RNAi) (Carvalho *et al.*, 2011). Nematodes at the fourth larval stage were grown on RNAi plates for 16 h at 20°C and then adult nematodes were dissected in 10 μl Shelton's growth media (SGM; Shelton and Bowerman, 1996) to prevent the permeabilized embryos from lysing due to osmotic shock. Embryos were mounted between a microscope slide and an 18 × 18 mm coverslip using 25-μm beads as spacers to make a small chamber (Yan *et al.*, 2021). A short time-lapse movie was recorded of untreated embryos until cortical flows had started. Then 20 μl of SMG with 10 μg/ml Latrunculin A were flowed into the mounting chamber. The effect of the drug was then followed with longer time-lapse imaging.

SI TIRF and spinning-disk imaging

Confocal movies were acquired with a Nikon Eclipse Ti spinning-disk, confocal microscope with an Apo TIRF 100× oil objective lens (NA 1.49), a Yokogawa CSU-X spinning-disk scan head, and a

Hamamatsu ORCA-Flash4.0 CMOS camera. A 488-nm laser (5mW power with a 525/50 bandpass emission filter) and a 561-nm laser (of 2 mW power with a 568-nm long pass filter) were used, respectively, for imaging GFP and mKate.

The thickness of the optical section for this microscope setup was calculated to be 0.5649 µm by considering the full width at half maximum of the point spread function along the axial direction according to Naredi-Rainer *et al*. (2013),

$$FWHM_{axial} = \sqrt{\left(\frac{0.88\lambda_{AV}}{n-\sqrt{n^2-NA^2}}\right)^2 + \left(\frac{\sqrt{2nPH}}{NA}\right)^2}$$

where λ_{AV} is an average of the excitation (λ_{AV}) and emission (λ_{AV}) wavelengths and given by

$$\lambda_{AV} = \sqrt{2\frac{\lambda_{em}\lambda_{exc}}{\lambda_{exc}^2\lambda_{em}}}$$

where *n* is the refractive index for the immersion oil used (1.51), *NA* is the numerical aperture of the lens (1.49), and *PH* is the diameter of the pinhole as it appears in object space (0.4550 µm using a spinning disk with pinhole diameters of 50 µm; Naredi-Rainer *et al*., 2013).

Superresolution images were acquired with a DeltaVision OMX SR in its SI TIRF mode with a pco.edge 5.5 sCMOS camera and an Olympus PlanApo 60× oil objective lens (*NA* = 1.42). Immersion oil of 1.516 refractive index was used. In this imaging mode, nine images were acquired for each frame in each channel. The nine exposures per frame were aligned and reconstructed using the softWoRx software. The 488-nm laser (with a 528/24 emission filter, 7-ms exposure time—for a single image—and 75% of the laser power) was used for imaging GFP-labeled filaments. mKate was imaged by a 561-nm laser (with a 609/18.5 emission filter and 20-ms exposure time with 50% laser power or 25-ms exposure time with 40% laser power). The shortest possible time intervals of 0.4 s for two channel movies and 90–100 ms for one channel movies were used.

Image preprocessing

Movies of the embryos were rotated in Fiji (Schindelin *et al*., 2012) such that their AP axis was horizontal with the posterior side on the right. The first frame where the NMY-2::GPF intensity in the equator increased above baseline was set as the time when ring assembly started. This time was used for temporal alignment of movies for later processing. A mask of the largest rectangular region of the cortex in spot was drawn manually and, depending on the analysis, subdivided into anterior side and posterior halves, divided into 10 or 18 equally sided bins along the AP axis, or divided into a region where the cytokinetic ring formed. For the data *let-502* RNAi in Figure 4D, the anterior cap extends into the posterior half of the cell and therefore overlaps with the equator where the ring forms giving rise to the unexpectedly high values seen in the posterior ROI (see Figure 4B).

NMII spots segmentation and tracking

Individual NMII spots were segmented and their position was tracked over time using a customized version of the Mosaic Particle Tracker plugin in Fiji (Sbalzarini and Koumoutsakos, 2005). Mosaic calculates the intensity of particles as the sum of the raw intensities of a fixed number of pixels allocated to each particle. For the particle detection in spinning-disk images, a radius of 3 pixels was set and particles falling below the upper sixth percentile of all pixel intensities were excluded. For SI TIRF images these values were set to 2 pixels and 2%, respectively. The particles were linked together between different frames to make tracks. To do this, the algorithm of Brownian motion dynamics and a cutoff score of 0 were used throughout. Other parameters we set individually for each acquisition are as follows. For spinning-disk images with 100-ms intervals, a link range of three frames and a displacement of 2 pixels were used. For images with 5-s intervals, these parameters were set to three frames and 2 pixels. For SI TIRF images, a link range of two or three frames and a displacement of 1 or 10 pixels were used for images with 90-ms or 2-s intervals, respectively. The position and pixel intensity parameters for all detected NMII spots in each movie were listed together with their respective frame and trajectory number and then exported as a text file and analyzed as described below.

Image analysis

Data were analyzed using custom functions written in MATLAB version *9.6.0.1214997 (R2019a) Update 6* (MathWorks, Natick, MA). The NMII spot density and average intensity were calculated from the Mosaic output file. The density of the NMII spots in each ROI (or each bin along the AP axis) is the number of detected spots divided by the area of that ROI (or bin). The densities in each ROI (or bin) are averaged over all embryos of a condition (e.g., RNAi condition). NMII spot intensity is the sum of the intensity values of the pixels identified as particles, these values were then averaged over all spots in a spatial bins for all the embryos of a condition. NMII spot trajectories from SI TIRF movies are used only when the intensity is analyzed for a single spot over time (for example, for color-coded tracks) because the image reconstruction of SI TIRF microscopy renders the intensity value incomparable between samples. For cytoplasmic NMII intensity, the cell was first divided into ROIs according to the analysis needed, and then the mean intensity per pixel of the ROI was calculated. ROIs were made either with a custom MATLAB script and then divided into bins along the AP axis or as hand-drawn masks or masks made using the Ilastik image segmentation algorithm (Berg *et al*., 2019) which were then read by custom MATLAB scripts.

Colocalization of NMII and actin in the cytoplasm

Images of NMY-2::GFP and mKate::Lifeact were taken simultaneously with the images of these proteins in the cortical plane (Figure 1, A–D). The background was subtracted using the rolling ball method (100 pixels) and then denoised (theta = 6) and the brightness and intensity were adjusted in Fiji (ImageJ version 2.0.0-rc-65/1.51v, 2018; Schindelin *et al*., 2012). Unprocessed images were used to calculate a Pearson, linear correlation coefficient (using the "corr" command in MATLAB) between pixel intensity values from the NMY-2::GFP and mKate::Lifeact channels.

PIV

Cortical flow velocities were measured by performing PIV on the actin channel of the two-channel spinning-disk movies. To calculate the velocity, the PIVlab MATLAB algorithm was used (version 1.4, Thielicke and Stamhuis, 2014). A three-pass PIV was performed with a final interrogation window of 64 × 64 pixels and a final step size of 32 pixels. The flows were analyzed over 50–100 s after the onset of the ring formation. In 10 bins along the AP axis, cortical velocities were averaged spatially for each frame and then over all time frames for each embryo. Values were then averaged over all embryos in each condition and plotted for the posterior bins. To measure the flows during ring ingression, the PIV was performed as above except for the NMY-2::GFP channel for the period from maintenance phase to cytokinesis. The flow velocities are presented as vectors

showing the magnitude and direction of net flow overlaid on the microscopy picture.

ACKNOWLEDGMENTS

We thank Krysztof Gonciarz, Mosaic group from the MPI-CBG, Dresden for providing the customized version of the Mosaic particle tracker; Emmanuel Beaurepaire and Pierre Mahou from the Laboratory for Optics and Biosciences at Ecole Polytechnique, Paris for access to a OMX microscope; Anne-Cecile Reymann for useful discussions and invaluable support; Dora Polić for help with data analysis; and Teije Middelkoop and Jamie White for critical reading of the manuscript. S.W.G. was supported by the following grants from the DFG: SPP 1782, GSC 97, GR 3271/2, GR 3271/3, and GR 3271/4, and the European Research Council 281903 and 742712.

REFERENCES

Alvarado J, Sheinman M, Sharma A, MacKintosh FC, Koenderink GH (2013). Molecular motors robustly drive active gels to a critically connected state. Nat Phys 9, 591–597.

Beach JR, Bruun KS, Shao L, Li D, Swider ZRemmert K, Zhang Y, Conti MA, Adelstein RS, Rusan NM, *et al*. (2017). Actin dynamics and competition for myosin monomer govern the sequential amplification of myosin filaments. Nat Cell Biol 9, 85–93.

Beatty A, Morton DG, Kemphues K (2013). PAR-2, LGL-1 and the CDC-42 GAP CHIN-1 act in distinct pathways to maintain polarity in the *C. elegans* embryo. Development 140, 2005–2014.

Begasse ML, Hyman AA (2011). The first cell cycle of the *Caenorhabditis elegans* embryo: spatial and temporal control of an asymmetric cell division. Results Probl Cell Differ 53, 109–133.

Berg S, Kutra D, Kroeger T, Straehle CN, Kausler BX, Haubold C, Schiegg M, Ales J, Beier T, Rudy M, *et al*. (2019). ilastik: interactive machine learning for (bio)image analysis. Nat Methods 16, 1226–1232.

Billington N, Wang A, Mao J, Adelstein RS, Sellers JR (2013). Characterization of three full-length human Nonmuscle Myosin II paralogs. J Biol Chem 288, 33398–33410.

Blanchoin L, Boujemaa-Paterski R, Sykes C, Plastino J (2014). Dynamics, architecture, and mechanics in cell motility. Physiol Rev 94, 235–263

Breckenridge MT, Dulyaninova NG, Egelhoff TT (2009). Multiple regulatory steps control mammalian Nonmuscle Myosin II assembly in live cells. Mol Biol Cell 20, 338–347.

Brenner S (1974). The genetics of *Caenorhabditis elegans*. Genetics 77, 71–94.

Bringmann H, Hyman AA (2005). A cytokinesis furrow is positioned by two consecutive signals. Nature 436, 731–734.

Burnette DT, Shao L, Ott C, Pasapera AM, Fischer RS, Baird MA, Der Loughian C, Delanoe-Ayari H, Paszek MJ, Davidson MW, *et al*. (2020). A contractile and counterbalancing adhesion system controls the 3D shape of crawling cells. J Cell Biol 205, 83–96.

Carvalho A, Olson SK, Gutierrez E, Zhang KNoble LB, Zanin E, Desai A, Groisman AOegema K (2011). Acute drug treatment in the early *C. elegans* embryo. PLoS One 6, e24656.

Chanet S, Miller CJ, Vaishnav ED, Ermentrout B, Davidson LA, Martin AC (2017). Actomyosin meshwork mechanosensing enables tissue shape to orient cell force. Nat Commun 8, 15014.

Dechant R, Glotzer M (2003). Centrosome separation and central spindle assembly act in redundant pathways that regulate microtubule density and trigger cleavage furrow formation. Dev Cell 4, 333–344.

Descovich CP, Cortes DB, Ryan S, Nash J, Zhang L, Maddox PS, Nedelec F, Maddox AS (2018). Cross-linkers both drive and brake cytoskeletal remodeling and furrowing in cytokinesis. Mol Biol Cell 29, 622–631.

Dickinson DJ, Ward JD, Reiner DJ, Goldstein B (2013). Engineering the *Caenorhabditis elegans* genome using cas9-triggered homologous recombination. Nat Methods 10, 1028–1034.

Ding WY, Ong HT, Hara Y, Wongsantichon J, Toyama Y, Robinson RC, Nédélec F, Zaidel-Bar R (2017). Plastin increases cortical connectivity to facilitate robust polarization and timely cytokinesis. J Cell Biol 216, 1371–1386.

Etienne-Manneville S, Hall A (2002). Rho GTPases in cell biology. Nature 420, 629–635.

Fenix AM, Taneja N, Buttler CA, Lewisa J, Van Engelenburg SB, Ohi R, Burnette DT (2016). Expansion and concatenation of nonmuscle myosin IIA filaments drive cellular contractile system formation during interphase and mitosis. Mol Biol Cell 27, 1465–1478.

Goldstein B, Hird SN (1996). Specification of the anteroposterior axis in *Caenorhabditis elegans*. Development 122, 1467–1474.

Green RA, Paluch E, Oegema K (2012). Cytokinesis in animal cells. Annu Rev Cell Dev Biol 28, 29–58.

Gross P, Kumar KV, Goehring NW, Bois JS, Hoege C, Jülicher F, Grill SW (2018). Guiding self-organized pattern formation in cell polarity establishment. Nat Phys 15, 293–300.

Gubieda AG, Packer JR, Squires I, Martin J, Rodriguez J (2020). Going with the flow: insights from *Caenorhabditis elegans* zygote polarization. Philos Trans R Soc Lond B Biol Sci B 375, 20190555.

Guo M, Chandris P, Giannini JP, Trexler AJ, Fischer R, Chen J, Vishwasrao HD, Rey-Suarez IWu Y, Wu X, *et al*. (2018). Single-shot superresolution total internal reflection fluorescence microscopy. Nat Methods 15, 425–428.

Hoege C, Hyman AA (2013). Principles of PAR polarity in Caenorhabditis elegans embryos. Nat Rev Mol Cell Biol 14, 315–322.

Hu S, Dasbiswas K, Guo Z, Tee Y-H, Thiagarajan V, Hersen P, Chew T-L, Safran SA, Zaidel-Bar R, Bershadsky AD (2017). Long-range self-organization of cytoskeletal myosin II filament stacks. Nat Cell Biol 19, 133–141.

Jenkins N, Saam JR, Mango SE (2006). CYK-4/GAP Provides a localized cue to initiate anteroposterior polarity upon fertilization. Science 313, 1298–1301.

Jülicher F, Grill SW, Salbreux G (2018). Hydrodynamic theory of active matter. Rep Prog Phys 81, 076601.

Kamath RS, Ahringer J (2003). Genome-wide RNAi screening in *Caenorhabditis elegans*. Methods 30, 313–321.

Khaliullin RN, Green RA, Shi LZ, Gomez-Cavazos JS, Berns MW, Desai A, Oegema K (2018). A positive-feedback-based mechanism for constriction rate acceleration during cytokinesis in *Caenorhabditis elegans*. eLife 7, e36073.

Kumfer KT, Cook SJ, Squirrell JM, Eliceiri KW, Peel N, O'Connell KF, White JG (2010). CGEF-1 and CHIN-1 regulate CDC-42 activity during asymmetric division in the *Caenorhabditis elegans* embryo. Mol Biol Cell 21, 266–277.

Lecuit T, Lenne P-F, Munro E (2011). Force generation, transmission, and integration during cell and tissue morphogenesis. Annu Rev Cell Dev Biol 27, 157–184.

Leite J, Chan F-Y, Osório DS, Saramago J, Sobral AF, Silva AM, Gassmann R, Carvalho AX (2020). Equatorial Non-muscle Myosin II and Plastin cooperate to align and compact F-actin bundles in the cytokinetic ring. Front Cell Dev Biol 8, 1003–1018.

Levayer R, Lecuit T (2012). Biomechanical regulation of contractility: spatial control and dynamics. Trends Cell Biol 22, 61–81.

Lewellyn L, Carvalho A, Desai A, Maddox AS, Oegema K (2018). The chromosomal passenger complex and centralspindlin independently contribute to contractile ring assembly. J Cell Biol 193, 155–169.

Li Y, Munro E (2021). Filament-guided filament assembly provides structural memory of filament alignment during cytokinesis. Dev Cell 56, 2486–2500.

Maddox AS, Lewellyn L, Desai A, Oegema K (2007). Anillin and the Septins promote asymmetric ingression of the cytokinetic furrow. Dev Cell 12, 827–835.

Marston DJ, Higgins CD, Peters KA, Cupp TD, Dickinson DJ, Pani AM, Moore RP, Cox AH, Kiehart DP, Goldstein B (2016). MRCK-1 drives apical constriction in *C. elegans* by linking developmental patterning to force generation. Curr Biol 26, 2079–2089.

Mayer M, Depken M, Bois JS, Jülicher F, Grill SW (2010). Anisotropies in cortical tension reveal the physical basis of polarizing cortical flows. Nature 467, 617–621.

Motegi F, Sugimoto A (2006) Sequential functioning of the ECT-2 RhoGEF, RHO-1 and CDC-42 establishes cell polarity in *Caenorhabditis elegans* embryos. Nat Cell Biol 8, 978–985.

Munro E, Nance J, Priess JR (2004). Cortical flows powered by asymmetrical contraction transport PAR proteins to establish and maintain anterior-posterior polarity in the early *C. elegans* embryo. Dev Cell 7, 413–424.

Naganathan SR, Fürthauer S, Nishikawa M, Jülicher F, Grill SW (2014). Active torque generation by the actomyosin cell cortex drives left–right symmetry breaking. eLife 3, e04165.

Naredi-Rainer N, Prescher J, Hartschuh A, Lamb DC (2013). Confocal microscopy. In: Fluorescence Microscopy: From Principles to Biological Applications, ed. U Kubitscheck. Weinheim: Wiley-Blackwell.

Niederman R, Pollard TD (1975). Human platelet myosin. II. *In vitro* assembly and structure of myosin filaments. J Cell Biol 67, 72–92.

Nishikawa M, Naganathan SR, Jülicher F, Grill SW (2017). Controlling contractile instabilities in the actomyosin cortex. eLife 6, e19595.

Pacquelet A (2017). Asymmetric cell division in the one-cell *C. elegans* embryo: multiple steps to generate cell size asymmetry. In Asymmetric Cell Division in Development, Differentiation and Cancer. Results and Problems in Cell Differentiation, Springer, 115–140.

Piekny AJ, Mains PE (2002). Rho-binding kinase (LET-502) and myosin phosphatase (MEL-11) regulate cytokinesis in the early *Caenorhabditis elegans* embryo. J Cell Sci 115, 2271–2282.

Piekny AJ, Johnson J-LF, Cham GDMains PE (2003). The *Caenorhabditis elegans* nonmuscle myosin genes nmy-1and *nmy-2* function as redundant components of the *let-502*/Rho-binding kinase and *mel-11*/myosin phosphatase pathway during embryonic morphogenesis. Development 130, 5695–5704.

Pimpale LG, Middelkoop TC, Mietke A, Grill SW (2020). Cell lineage-dependent chiral actomyosin flows drive cellular rearrangements in early *Caenorhabditis elegans* development. eLife 9, e54930.

Pollard TD (2016). Actin and actin-binding proteins. In Cold Spring Harbor Perspectives in Biology, Vol. 8, ed. T D. Pollard and R D. Goldman, Cold Spring Harbor Laboratory Press, a018226.

Reymann A-C, Staniscia F, Erzberger A, Salbreux. G, Grill SW (2016). Cortical flow aligns actin filaments to form a furrow. eLife 5, e17807.

Rose L, Gönczy P (2014). Polarity establishment, asymmetric division and segregation of fate determinants in early *C. elegans* embryos, in WormBook, ed. The C. elegans Research Community, WormBook, doi/10.1895/wormbook.1.30.2, http://www.wormbook.org.

Salbreux G, Prost J, Joanny JF (2009). Hydrodynamics of cellular cortical flows and the formation of contractile rings. Phys Rev Lett 103, 058102.

Salbreux G, Charras G, Paluch E (2012). Actin cortex mechanics and cellular morphogenesis. Trends Cell Biol 22, 536–545.

Sbalzarini IF, Koumoutsakos P (2005). Feature point tracking and trajectory analysis for video imaging in cell biology. J Struct Biol 151, 182–195.

Schindelin J, Arganda-Carreras I, Frise E, Kaynig V, Longair M, Pietzsch T, Preibisch S, Rueden C, Saalfeld S, Schmid B, *et al*. (2012). Fiji: an open-source platform for biological-image analysis. Nat Methods 9, 676–682.

Schonegg S, Hyman AA (2006). CDC-42 and RHO-1 coordinate acto-myosin contractility and PAR protein localization during polarity establishment in *C. elegans* embryos. Development 133, 3507–3516.

Sellers JR (2000). Myosins: a diverse superfamily. Biochim Biophys Acta 1496, 3–22.

Shelton CA, Bowerman B (1996). Time-dependent responses to *glp-1*-mediated inductions in early *C. elegans* embryos. Development 122, 2043–2050.

Shutova MS, Spessott WA, Giraudo CG, Svitkina T (2014). Endogenous Species of Mammalian Nonmuscle Myosin IIA and IIB Include Activated Monomers and Heteropolymers. Curr Biol 24, 1958–1968.

Thielicke W, Stamhuis EJ (2014). PIVlab – toward user-friendly, affordable and accurate digital particle image velocimetry in MATLAB. J Open Res Softw 2, 1202–1210.

Timmons L, Court DL, Fire A (2001). Ingestion of bacterially expressed dsRNAs can produce specific and potent genetic interference in *Caenorhabditis elegans*. Gene 263, 103–112.

Tse YC, Piekny A, Glotzer M (2011). Anillin promotes astral microtubule-directed cortical myosin polarization. Mol Biol Cell 22, 3165–3175.

Tse YC, Werner M, Longhini KM, Labbe J-C, Goldstein B, Glotzer M (2012). RhoA activation during polarization and cytokinesis of the early *Caenorhabditis elegans* embryo is differentially dependent on NOP-1 and CYK-4. J Mol Biol Cell 23, 4020–4031.

Wissmann. A, Ingles J, McGhee JD, Mains PE (1997). *Caenorhabditis elegans* LET-502 is related to Rho-binding kinases and human myotonic dystrophy kinase and interacts genetically with a homolog of the regulatory subunit of smooth muscle myosin phosphatase to affect cell shape. Genes Dev 11, 409–422.

Wolfe BA, Takaki T, Petronczki M, Glotzer M (2009). Polo-like kinase 1 directs assembly of the HsCyk-4 RhoGAP/Ect2 RhoGEF complex to initiate cleavage furrow formation. PLoS Biol 7, e1000110.

Yan VT, Narayanan A, Jülicher F, Grill SW (2021). A condensate dynamic instability orchestrates oocyte actomyosin cortex activation. bioRxiv: doi.org/10.1101/2021.09.19.460784